Hybrid large-eddy simulation/Lagrangian filtered-density-function approach for simulating turbulent combustion

Venkatramanan Raman [a,*], Heinz Pitsch [a], Rodney O. Fox [b]

[a] *Center for Turbulence Research, Stanford University, Stanford, CA 94305, USA*
[b] *Department of Chemical Engineering, Iowa State University, Ames, IA 50010, USA*

Abstract

A consistent hybrid large-eddy simulation/filtered-density-function approach (LES-FDF) is formulated for variable-density low-Mach-number flows. The LES-FDF approach has been proposed as a suitable method for finite-rate-chemistry-based predictive modeling of turbulent reactive flows. Due to the large computational grid associated with LES, use of Lagrangian schemes is numerically expensive. In this work, a highly efficient parallel Lagrangian implementation is used for the simulation of a nonpremixed flame. This bluff-body-stabilized flame is characterized by complex flow fields that interact strongly with the combustion mechanism. A LES grid size of 1 million computational cells and roughly 15 million notional particles is used to simulate a time-accurate variable-density flow. The hybrid approach predicts the time-averaged velocity and root mean square (RMS) velocity components quite accurately. Species profiles including hydroxyl radical compare well with experimental data. Consistency and accuracy are established by comparing particle and Eulerian density, mixture fraction, and RMS mixture fraction fields. Scalar FDFs at select locations are shown to be well approximated by the presumed beta function used in typical combustion LES.

1. Introduction

Predictive modeling of turbulent combustion has high practical value in diverse areas such as aircraft engines, power generation, and modeling chemical reactors. The phenomenal increase in computational power in the past decade has made many of these flow configurations numerically accessible. Nevertheless, the strong interaction of turbulence with complex chemistry has posed a formidable challenge [1]. Significant advances in modeling passive turbulent flows have been possible with the development of the large-eddy simulation (LES) technique [2]. LES directly solves for the large scales of turbulent motion and models the subfilter or the unresolved components. Since the interaction of turbulent mixing with combustion chemistry occurs at subfilter-length scales, reactions need to be completely modeled. In practical terms, this implies that the scalar transport equation for a reactive scalar cannot be solved directly since the reaction source term cannot be closed in terms of the mean reactive scalars alone.

* Corresponding author.
E-mail address: vraman@stanford.edu (V. Raman).

Combustion models for LES of nonpremixed configurations are directly derived from corresponding (RANS) models. Since LES resolves the large turbulence scales, such models have been found to be quite effective in modeling reactions [3]. Most models currently used in LES of turbulent combustion use a conserved-scalar approach based on the mixture fraction. In particular, the steady laminar flamelet model (SLFM) uses the filtered mixture fraction and the dissipation rate of the mixture fraction to describe the thermochemical state. For fast chemistry with no extinction, this model has been found to be quite accurate [1,4]. The key advantage of the steady laminar flamelet approach is that the reactive scalars can be parameterized in terms of the mixture fraction and the scalar dissipation rate and pretabulated. This table can be used to look up density or any other scalar values during the LES computation, thereby reducing the computational requirements to solving for the mixture fraction alone. The conditional moment closure (CMC) model has similarly been applied to turbulent combustion configurations with little or no extinction [5–7]. CMC requires an additional set of equations to be solved in the mixture fraction dimension but can be decoupled in the case of steady state RANS calculations. More detailed models for combustion, such as the unsteady flamelet model and transient CMC calculation, are indeed computationally expensive and are not commonly used.

Although the SLFM approach is quite efficient, its use is limited to reaction schemes that are in the fast-chemistry regime and evolve on a two-dimensional manifold. Departures from such ideality can occur due to local extinction or slow chemistry. For such cases, additional scalars need to be used to describe reaction. The most generalized model for such a scenario is the transported filtered-density-function (FDF) approach, where the joint scalar probability density function (PDF) is evolved. A transport equation for the one-point, one-time, joint velocity–scalar PDF can be formulated [8]. However, this equation cannot be solved directly using conventional Eulerian discretization methods due to its high dimensionality [9]. Usually, an equivalent Lagrangian system using a set of stochastic differential equations is evolved. This can be shown to describe the original FDF transport equation discretely [2,10]. The FDF approach requires closure for the conditional mixing term that appears in the transport equation. Although several models have been proposed in Refs. [11–15], none of the current models satisfies all consistency requirements for micromixing [16]. Since LES directly solves for all large scales, it is expected that the influence of the micromixing model will be smaller than that in a RANS simulation.

Use of particle schemes have so far been limited to simple flow configurations primarily due to the computational cost and numerical stability issues. With recent advances in computational power, the computational expense might be overcome for many practical problems in the foreseeable future. The numerical stability issue in solving joint velocity–scalar FDFs arises from the need for gradient fields based on particle properties [2,16]. Due to the stochastic nature of the solution method, such fields are inherently noisy and can lead to numerical instabilities. Recently, a novel hybrid scheme that exploits the advantages of particle and Eulerian methods has been proposed [17]. In such methods, an Eulerian flow solver is used to obtain the velocity and turbulence fields. The Lagrangian scheme can then evolve either the joint velocity–composition FDF or the joint composition FDF [2]. In either case, the mean velocity and pressure fields are obtained from the Eulerian solver, thereby reducing statistical errors. The coupling between the Eulerian and the Lagrangian schemes is through the transfer of mean fields used to advance the respective equations. The Eulerian solver provides the filtered velocity and turbulence fields which are used to advance the particles in physical and compositional spaces. The particle properties are then used to evaluate a new density field that is used by the Eulerian solver to advance the flow field. The hybrid approach has been used to simulate several experimental configurations with reasonable accuracy [17–19]. It is noted here that almost all known simulations use a steady state approach. A loosely coupled approach [20] where the steady state nature of the solver is used to minimize the statistical errors can be adopted.

Such hybrid schemes have been extended to LES methods also [21–23]. Since LES methods are inherently transient, maintaining statistical accuracy of the Lagrangian scheme in the temporal sense is of paramount importance. Simplifying assumptions used in steady-state-based approaches are not valid in the transient LES simulations. In addition, LES grids are at least an order of magnitude bigger than typical RANS grids, implying that the total number of particles in the domain could exceed several millions. Simulations of simple flow configurations using the LES-FDF scheme have shown encouraging results and good agreement with experimental and (DNS) fields [21,22]. However, extension to flows with strong density gradients and complex flow fields is nontrivial. In the present study, we use a joint composition FDF which uses the LES flow fields to evolve the particles in physical and compositional space. A consistent stable algorithm needs to be formulated to ensure temporal and spatial accuracy.

For the purposes of this study, the nonpremixed methane–hydrogen flame configuration studied experimentally at the University of Sydney [24] will be used to demonstrate the feasibility and accuracy of such coupled schemes. This particular configuration was chosen due to the complex flow fields exhibited by bluff-body-stabilized flames. The flow is highly transient and the flame dynamics can be captured only by a time-dependent simulation. This configuration exhibits a low level of extinction and should be well represented by a laminar flamelet model [25].

In general it has been observed that the near-bluff-body mixture fraction profile can be reasonably reproduced by the simulation. However, the flow exhibits vortex shedding in the outer shear layer that interacts with the flame structure further downstream. This experimental flame has been studied numerically in the past with only limited success due to the complex flow structure and the strong interaction of the flame with turbulence [7,19,25]. It is expected that LES will provide a better resolution of the flow features than RANS-based methods.

The focus of the current work is to establish the LES-FDF scheme as a practical simulation tool for complex flow configurations. The first part of this article will detail the numerical algorithms, consistency requirements, and implementation issues. The computational grid used here is typical of LES calculations. It will serve to identify the computational cost of particle schemes for practical configurations.

2. Governing equations for hybrid approach

The hybrid scheme consists of two separate solvers—the LES flow solver and the Lagrangian FDF solver. The two solvers are coupled through a feedback mechanism which transfers reaction information to the flow solver [20] (Fig. 1). When using the low-Mach-number approximation, it is inherently assumed that the change in flow is caused only by density changes arising from reactions. Hence all feedback mechanisms pass the Lagrangian filtered density field to the flow solver. This can be accomplished by
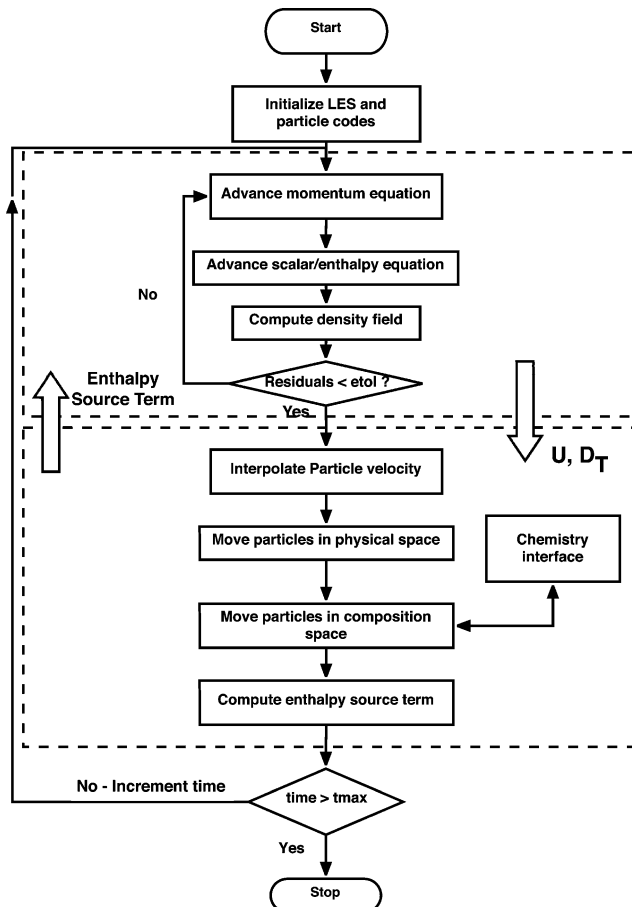

Fig. 1. Flowchart showing the coupled LES-FDF simulation with feedback.

a direct feedback [20] or by indirect transfer [19]. In the latter case, an additional enthalpy equation is solved in an Eulerian manner. The exact source term for this equation is obtained using the particle thermochemical properties. The following sections describe the mathematical formulations of the various components.

2.1. Eulerian LES flow solver

The LES technique solves for the resolved scales of the turbulent flow, also known as the filtered quantities. For variable-density flows, a Favre-filtered variable can be defined such that

$$\tilde{Q} = \frac{1}{\bar{\rho}} \int \rho Q G(\mathbf{y} - \mathbf{x}) \, d\mathbf{y}, \tag{1}$$

where Q is any scalar field, ρ and $\bar{\rho}$ are the unfiltered and filtered density, respectively, and G is a filtering kernel defined on the physical space. In all known practical LES simulations, the filter is a box filter which implies that the filter is defined by the grid itself. The kernel definition satisfies the criterion that

$$\bar{\rho} = \int \rho G(\mathbf{y} - \mathbf{x}) \, d\mathbf{y}. \tag{2}$$

Applying the above definition to the Navier–Stokes equation leads to the following filtered momentum equations.

$$\frac{\partial \bar{\rho}}{\partial t} + \frac{\partial \bar{\rho} \tilde{u}_i}{\partial x_i} = 0 \tag{3}$$

and

$$\frac{\partial \bar{\rho} \tilde{u}_i}{\partial t} + \frac{\partial \bar{\rho} \tilde{u}_i \tilde{u}_j}{\partial x_j} = -\frac{\partial \tilde{P}}{\partial x_i} + \frac{\partial \tau_{ij}}{\partial x_j} + \frac{\partial T_{ij}}{\partial x_j}, \tag{4}$$

where τ_{ij} is the viscous stress tensor given by

$$\tau_{ij} = \tilde{\mu} \left(\frac{\partial \tilde{u}_i}{\partial x_j} + \frac{\partial \tilde{u}_j}{\partial x_i} - \frac{2}{3} \frac{\partial \tilde{u}_k}{\partial x_k} \delta_{ij} \right) = 2\tilde{\mu} \tilde{S}_{ij}, \tag{5}$$

and $T_{ij} = \bar{\rho} \tilde{u}_i \tilde{u}_j - \bar{\rho} \widetilde{u_i u_j}$ denotes the subfilter stresses. $\tilde{\mu}$ is obtained from the flamelet lookup table. The transport equation for the conserved scalar can be written as

$$\frac{\partial \bar{\rho} \tilde{Z}}{\partial t} + \frac{\partial \bar{\rho} \tilde{u}_j \tilde{Z}}{\partial x_j} = \frac{\partial}{\partial x_j} \left(\bar{\rho} \tilde{D} \frac{\partial \tilde{Z}}{\partial x_j} \right) + \frac{\partial M_{Z,j}}{\partial x_j}, \tag{6}$$

where $M_{Z,j} = \bar{\rho} \tilde{u}_j \tilde{Z} - \bar{\rho} \widetilde{u_j Z}$. The diffusion term can be approximated by

$$\overline{\frac{\partial}{\partial x_j} \left(\rho D \frac{\partial Z}{\partial x_j} \right)} = \frac{\partial}{\partial x_j} \left(\bar{\rho} \tilde{D} \frac{\partial \tilde{Z}}{\partial x_j} \right), \tag{7}$$

where $\tilde{D}$ is obtained from the flamelet lookup table. For the sake of simplicity, $\tilde{D}$ is written as D henceforth. Both T_{ij} and $M_{Z,j}$ should require closure models. Several models have been proposed [26,27]. Most

commonly used are the gradient-diffusion-hypothesis-based models [26,28]. The subfilter stress is then modeled using

$$\left(T_{ij} - \frac{\delta_{ij}}{3} T_{kk} \right) = 2\mu_t \left(\tilde{S}_{ij} - \frac{\delta_{ij}}{3} \tilde{u}_{kk} \right). \tag{8}$$

The eddy viscosity μ_t is obtained using the Smagorinsky model [26] as

$$\mu_t = \bar{\rho} C_s \Delta^2 \tilde{S}, \tag{9}$$

where $\tilde{S} = \sqrt{2\tilde{S}_{ij} \tilde{S}_{ij}}$ is the magnitude of the strain rate and Δ is the characteristic width of the filter. The coefficient C_s is determined using a dynamic procedure [29,30]. The subfilter scalar flux is also modeled using a gradient-diffusion hypothesis as

$$M_{Z,j} = \bar{\rho} D_t \frac{\partial \tilde{Z}}{\partial x_j}, \tag{10}$$

where D_t is the eddy diffusivity. The eddy diffusivity is computed using a formulation similar to that of the eddy viscosity

$$D_t = C_z \Delta^2 \mathcal{S}, \tag{11}$$

where C_z is determined dynamically [29]. It is apparent that the eddy viscosity and diffusivity are modeled using the same functional form and differ only in the coefficients [31]. The ratio C_z/C_s then gives the turbulent Schmidt number.

The FDF transport equation (to be described in Section 2.2) can be used to obtain moment equations of the scalars [16]. The zeroth moment is the continuity equation while the first moment yields the filtered scalar equation. In a similar spirit, a moment equation for the subfilter variance can also be formulated. Due to numerical limitations, computation of such small quantities invariably lead to large errors. Instead, a resolved-scale quantity, namely the second moment of the mixture fraction is computed. The subfilter variance field can then be obtained using a simple algebraic relationship. The key advantage in using this formulation is that the $\widetilde{Z^2}$ equation does not contain any source term and is deemed more accurate.

$$\frac{\partial \bar{\rho} \widetilde{Z^2}}{\partial t} + \frac{\partial \bar{\rho} \tilde{u}_j \widetilde{Z^2}}{\partial x_j}$$
$$= \overline{\frac{\partial}{\partial x_j} \left(\rho D \frac{\partial Z^2}{\partial x_j} \right)} + \frac{\partial M_{Z^2,j}}{\partial x_j} - \bar{\rho} \tilde{\chi}, \tag{12}$$

where $M_{Z^2,j} = \bar{\rho} \tilde{u}_j \widetilde{Z^2} - \bar{\rho} \widetilde{u_j Z^2}$. This term is modeled similar to $M_{Z,j}$ (Eq. (10)). The diffusion term is closed similar to Eq. (7).

The subfilter variance can then be defined as

$$\widetilde{Z''^2} = \widetilde{Z^2} - \tilde{Z}^2. \tag{13}$$

The dissipation term, $\tilde{\chi}$, is defined using a turbulent-diffusivity-based time scale [21]:

$$\bar{\rho}\tilde{\chi} = \overline{2\rho D\nabla Z\nabla Z} = 2\frac{\bar{\rho}(D+D_T)}{\Delta^2}\widetilde{Z''^2}. \qquad (14)$$

It is noted here that in LES of reacting flows, the subfilter variance is usually computed using a dynamic procedure [32]. Such a procedure inherently assumes that the physical transport terms in the variance equation are negligible and that local production is exactly balanced by local dissipation. Such a model will be inconsistent with the FDF representation where the particle evolution equations take into account the transport terms also. Hence, in this work, the second-moment equation is used to obtain the subfilter variance such that none of the transport terms are neglected. Numerical implementation of the above set of equations will be discussed later.

2.2. Lagrangian FDF system

The filtered-density function in LES is analogous to the joint composition PDF used for RANS-based simulations. For variable-density flows, the filtered mass density function (FMDF) [21] can be defined as

$$F_L(\boldsymbol{\psi};\mathbf{x},t) = \int\limits_{-\infty}^{+\infty} \rho(\mathbf{y},t)\xi\big[\boldsymbol{\psi},\boldsymbol{\phi}(\mathbf{y},t)\big]G(\mathbf{y}-\mathbf{x})\,d\mathbf{y} \tag{15}$$

and

$$\xi\big[\boldsymbol{\psi},\boldsymbol{\phi}(\mathbf{y},t)\big] = \delta\big[\boldsymbol{\psi}-\boldsymbol{\phi}(\mathbf{y},t)\big], \tag{16}$$

where δ is an N-dimensional delta function for an N-species system and $\boldsymbol{\psi}$ is the random variable in the composition domain. Equivalent to Eq. (2), the FMDF yields the following property:

$$\int\limits_{-\infty}^{+\infty} F_L\,d\boldsymbol{\psi} = \int\limits_{-\infty}^{+\infty} \rho(\mathbf{y},t)G(\mathbf{y}-\mathbf{x})\,d\mathbf{y} = \bar{\rho}. \tag{17}$$

Similarly, the filtered mean of any scalar Q_ϕ can be defined as

$$\begin{aligned}
\tilde{Q}_\phi &= \int\limits_{-\infty}^{+\infty} Q_\phi(\boldsymbol{\psi},\mathbf{y},t)F_L\,d\boldsymbol{\psi} \\
&= \frac{1}{\bar{\rho}}\int\limits_{-\infty}^{+\infty} \rho(\mathbf{y},t)Q_\phi(\mathbf{y},t)G(\mathbf{y}-\mathbf{x})\,d\mathbf{y}.
\end{aligned} \tag{18}$$

Using these definitions, the transport equation for the joint composition FDF can be written as [21,22]

$$\begin{aligned}
&\frac{\partial F_L}{\partial t} + \frac{\partial}{\partial\mathbf{x}}(\tilde{\mathbf{u}}F_L) + \frac{\partial}{\partial\mathbf{x}}\big(\widetilde{\mathbf{u}'|\boldsymbol{\psi}}\,F_L\big) \\
&\quad = -\frac{\partial}{\partial\boldsymbol{\psi}}\left[\left(\frac{1}{\bar{\rho}}\overline{\nabla\cdot\rho D\nabla\boldsymbol{\phi}|\boldsymbol{\psi}} + \mathbf{S}(\boldsymbol{\psi})\right)F_L\right], \quad (19)
\end{aligned}$$

where $\widetilde{\mathbf{u}'|\boldsymbol{\psi}}$ is the subfilter velocity fluctuation conditioned on the scalar, $\overline{\nabla\cdot\rho D\nabla\boldsymbol{\phi}|\boldsymbol{\psi}}$ is the conditional micromixing term, and $\mathbf{S}$ is the reaction source term. The conditional velocity term is modeled using the gradient-diffusion hypothesis to give

$$\widetilde{u'_j|\boldsymbol{\psi}}\,F_L = -\bar{\rho}D_T\frac{\partial F_L/\bar{\rho}}{\partial x_j}. \tag{20}$$

The conditional mixing term requires modeling and has been the focus of research in PDF methods [16]. Based on theoretical considerations, a set of constraints can be specified for any mixing model to truly represent the micromixing terms [33]. However, none of the current models satisfies all the requirements [2,16]. Although several models have been used in practical simulations [11–14], the interaction-by-exchange-with-the-mean (IEM) model is most commonly employed [12]. Here we use the IEM model specified as

$$\overline{\nabla\cdot\rho D\nabla\boldsymbol{\phi}|\boldsymbol{\psi}} = \nabla\cdot\bar{\rho}D\nabla\tilde{\boldsymbol{\phi}} - \frac{\bar{\rho}C_\phi}{\tau}(\boldsymbol{\psi}-\tilde{\boldsymbol{\phi}}), \tag{21}$$

where C_ϕ is the scalar-to-mechanical time-scale ratio and τ is a turbulence time scale. In the present study we set C_ϕ to be 2 [1] and we use a turbulent-diffusivity-based time scale [21]

$$\tau = \frac{2\Delta^2}{(D+D_T)}, \tag{22}$$

where Δ is the local filter width. If the FDF transport equation (Eq. (19)) is multiplied by ψ and integrated over the composition space, the scalar transport equation for the filtered mean can be obtained. In the absence of a reaction source term, this equation will reduce to the conserved scalar transport equation (Eq. (6)). The mixing time scale described above is consistent with the scalar dissipation rate defined in Eq. (14). The second-moment equation for the mixture fraction, obtained by multiplying the FDF transport equation (Eq. (19)) by ψ^2 and integrating over composition space, will be identical to Eq. (12).

The FDF transport equation is a high-dimensional equation. For a system described by N thermochemical variables evolving in three spatial dimensions with temporal variations, this equation spans $(N+4)$ dimensions. Conventional finite-different/finite-volume-based discretization schemes are not tractable for $N > 1$ [16]. Typical hydrocarbon chemistry will involve upward of 20 chemical species to capture the fundamental dynamics of the combustion process. To solve the FDF transport equation, an equivalent particle system is defined such that the particles evolve using stochastic differential equations in time and space [9,10]. The Lagrangian system scales linearly with the number of dimensions [2]. The equivalence between the Lagrangian FDF conditional on particle

initial positions that is evolved by the particle and the Eulerian FDF is established if the following criterion is satisfied [16]: Given an initial spatial distribution of particles that is directly proportional to the fluid density distribution, the particle distribution will evolve according to the fluid density, ensuring that, at any given time, the fluid density ($\bar{\rho}$) and the particle distribution ($F_{\mathbf{x}}^*$) correspond to each other:

$$F_{\mathbf{x}}^* \propto \bar{\rho}. \tag{23}$$

The above condition will ensure that the continuity equation is satisfied. It can then be shown that all higher moments of the scalars will correspond directly to the Eulerian scalar transport equations as implied by the FDF transport equation. In turn, this implies that the Lagrangian one-point FDF averaged over all realizations will yield the Eulerian one-point FDF that evolves according to Eq. (19).

The particles are defined such that they are uniformly distributed in the computational domain but are initialized with individual weights that are proportional to local fluid mass. The evolution in physical space is through transport equations that use the filtered flow field from the LES solver:

$$d\mathbf{x}^* = \left[\tilde{\mathbf{u}} + \frac{1}{\bar{\rho}} \nabla \bar{\rho}(D + D_T) \right] \Delta t \\ + \sqrt{2(D + D_T)} \, d\mathbf{W}, \tag{24}$$

where $\mathbf{x}^*$ is the instantaneous particle position and $d\mathbf{W}$ is the Wiener diffusion term characterized by a Gaussian process with zero mean and variance of Δt, where dt is the time step of the process. Transport in composition space is through mixing and reaction:

$$d\boldsymbol{\psi} = -\frac{C_\phi}{\tau}(\boldsymbol{\psi} - \tilde{\boldsymbol{\phi}}) \, \Delta t + \mathbf{S}(\boldsymbol{\psi}) \, \Delta t. \tag{25}$$

The Eulerian quantities can be computed by weighted means of the particle properties in each computational cell. In general, the composition array also includes the enthalpy or temperature so that the entire thermochemical state of the fluid can be described. In this study, the laminar flamelet model is used to describe the chemistry. By assumption, the mixture fraction and the mean scalar-dissipation rate in the computational cell determine the thermochemical state of the particle. Section 2.3 details the feedback mechanism used to couple the LES flow solver and the Lagrangian FDF solver through the definition of an enthalpy.

2.3. Feedback system

Before the feedback mechanism is described, it is important to understand the thermochemical state implied by the FDF system and the Eulerian LES solver.

In all hybrid approaches, there is redundancy of the variables solved [20]. Such redundant fields can be used to ensure consistency between the different components of the solver. In a composition-FDF-based simulation, the thermochemical density is used to ensure that the solver is accurate. In addition, when using laminar flamelet chemistry, a conserved scalar can be used to ensure consistency since the transport equation for a conserved scalar is closed and does not require subfilter information for its evolution.

In the current implementation, density can be evaluated using three different redundant quantities. Each particle in the computational domain carries a weight, w_i, and mixture fraction Z_i, where the subscript i refers to some consistent numbering that marks all the particles in a computational cell. Based on the assumption of laminar flamelet chemistry, the density can be evaluated using

$$\rho_i = \rho(Z_i, \tilde{\chi}), \tag{26}$$

where ρ denotes the flamelet table and $\tilde{\chi}$ is the modeled scalar-dissipation rate in the computational cell. The mean density in a given cell can then be computed as

$$\frac{1}{\bar{\rho}} = \frac{\sum_{i=1}^{N_p} w_i / \rho_i}{\sum_{i=1}^{N_p} w_i}, \tag{27}$$

where N_p denotes the number of particles in the computational cell. Initially, the particle weights are proportional to the density, so that the above relation will trivially hold for equally weighted particles. However, as the particles evolve through the stochastic equations, this direct relation is not strictly satisfied and is subject to statistical errors. A weaker condition can be specified using the continuity equation such that the sum of the particle weights is proportional to the local density at all times:

$$\sum_{i=1}^{N_p} w_i \propto \bar{\rho}, \tag{28}$$

where the proportionality constant is invariant with time and is exactly equal to the local cell volume. Due to the stochastic nature of the algorithm, this proportionality can be satisfied only within statistical errors. For steady state flows, time-averaging will remove the statistical noise and should yield a time-invariant proportionality constant.

The density field obtained from the particles $\bar{\rho}$ is used in evolving the Eulerian density field, $\bar{\rho}_{fv}$. This is given as

$$\bar{\rho}_{fv}^{t+1} = \bar{\rho}_{fv}^t + \mathcal{L} \left[\frac{(\bar{\rho}^{t+1} - \bar{\rho}_{fv}^t)}{\Delta t} \right] \Delta t, \tag{29}$$

where the superscript t refers to the time state and $\mathcal{L}$ is a spatial filtering operator used to reduce large spikes in the density change arising from statistical fluctuations. If the operator is removed at any step, the Eulerian density field will readjust to the particle field in a single time step as defined by the above equation. However, even for simple flows, the statistical noise in the particle-based density fields will render the simulation completely inaccurate and numerically unstable. Hence, direct feedback of the density through the equation described above is infeasible. It was found that increasing the number of particles reduced this noise, but, to obtain a stable feedback loop, the number of particles required is prohibitively expensive.

To overcome this problem, here we have used the enthalpy transport equation [34]. Following Muradoglu et al. [34], we define the equivalent enthalpy, h, as

$$h(\boldsymbol{\psi}) = \frac{\gamma}{\gamma - 1} \frac{P_0}{\rho(\boldsymbol{\psi})}, \tag{30}$$

where γ is the ratio of the specific heats and P_0 is the operating pressure. Since the equivalent enthalpy is a function only of the local thermochemical composition, the transport equation for h can be derived from the FDF transport equation.

$$\frac{\partial \bar{\rho}\tilde{h}}{\partial t} + \frac{\partial}{\partial x_j}(\bar{\rho}\tilde{u}_j \tilde{h}) = \frac{\partial}{\partial x_j} \bar{\rho}(D + D_T)\frac{\partial}{\partial x_j}(\tilde{h})$$
$$+ \bar{\rho}\left(\widetilde{h_\alpha S_\alpha} - \frac{1}{2\tau} C_\phi \widetilde{h_\alpha \phi_\alpha''} \right) \tag{31}$$

and

$$h_\alpha = \frac{\partial h}{\partial \phi_\alpha}, \tag{32}$$

where $\alpha = 1$ and N is the length of the composition array. It is evident that the physical transport terms in this equation can be treated in the same way as that of a conserved scalar equation. The source terms, however, are not known and need to be provided by the FDF solver. With regard to the particle properties, the source term is actually the change of enthalpy of the particles due to reaction and mixing [34]:

$$\widetilde{S_h} = \bar{\rho}\left(\widetilde{h_\alpha S_\alpha} - \frac{1}{2\tau} C_\phi \widetilde{h_\alpha \phi_\alpha''} \right). \tag{33}$$

The exact computation of this enthalpy source term will be discussed later. Once the equivalent enthalpy is known, the density field is found using the relation obtained by filtering Eq. (30),

$$\bar{\rho} = \frac{\gamma}{\gamma - 1} \frac{P_0}{\tilde{h}}, \tag{34}$$

where the low-Mach-number assumption has been used to remove the pressure fluctuations. This density field is then used in Eq. (29) without the filtering

operation. It is found that this feedback mechanism is numerically stable and does not lead to large spikes in the $d\bar{\rho}/dt$ term that appears in the continuity equation.

In summary, the governing equations for the hybrid approach have been provided. The LES flow solver obtains Favre-filtered velocity fields that are then used by the Lagrangian solver to advance the particles. The density field is used to modify the flow in the domain due to reactions. Direct feedback of the density field leads to numerical instability due to the inherent statistical noise in Lagrangian mean fields. The enthalpy transport equation is used to reduce this statistical noise by indirectly evolving the density field. The particle properties are used to evaluate the exact source term for the enthalpy equation, which is then used to solve for the filtered enthalpy field using finite-volume discretization methods. Based on this filtered enthalpy field, the local filtered density field can be evaluated. Such an approach reduces the large spikes in density change observed when direct density feedback is used. The next section details the numerical implementation of the individual flow solvers.

3. Numerical implementation

As detailed in Section 2.3, the hybrid solver involves three separate components. The LES flow solver is solved on a Eulerian grid using finite-volume-based discretization. Though Lagrangian schemes are conventionally grid-free simulations [16], in the present study, a tighter grid-based control is used to reduce statistical inaccuracies. The last component is the coupling algorithm that transfers information between the two transport solvers.

3.1. LES solver

The finite-volume-based LES flow solver is cast in a cylindrical coordinate system [32]. Energy-conserving discretization schemes are used for the momentum equations. The subfilter stress terms are closed using dynamic models [35]. An Eulerian scalar-transport algorithm is also implemented using the QUICK scheme [36]. The variable-density formulation follows a low-Mach-number approximation where the density is updated using an external solver. The updated density is then used to advance the momentum and scalar equations using a multi-step temporal algorithm [32]. The discretization in physical space is made implicit in the radial and azimuthal direction using a factorization scheme [37]. This removes the dependence of the (CFL) number on the radial direction that can otherwise drastically reduce the time step used. The LES solver uses

domain-decomposition-based parallelization to accelerate computation.

For the sake of comparison, the beta-function-presumed PDF-based scalar field values are also evaluated. The filtered mixture-fraction equation and the second-moment equation are used to obtain the filtered scalar values. The subfilter mixture fraction PDF is assumed to be a beta function [38].

$$\tilde{Q}(\tilde{Z}, \widetilde{Z''^2}, \tilde{\chi})$$
$$= \frac{1}{\bar{\rho}} \int_0^1 \rho(\xi, \tilde{\chi}) Q(\xi, \tilde{\chi}) P(\xi; \tilde{Z}, \widetilde{Z''^2}) \, d\xi, \qquad (35)$$

where ξ is the sample-space variable corresponding to the mixture fraction and the subfilter variance $\widetilde{Z''^2}$ is defined by Eq. (13), and $P(\xi; \tilde{Z}, \widetilde{Z''^2})$ is the beta-function. It is noted here that this evaluation is used strictly for the comparison only. All density and enthalpy source term calculations are based on particle properties where the subfilter FDF is evolved and does not have a presumed form.

3.2. Particle scheme

The Lagrangian solver represents the fluid using a set of notional particles [9]. Typical LES grids comprise 0.5–2 million computational volumes, which translates to roughly 5–25 million particles in the entire computational domain. Such a large number of particles demands efficient algorithms and robust parallelism. Below, the individual components of the algorithm are briefly described. Every particle is initialized in the domain with a weight corresponding to the average fluid mass assuming a nominal particle number density. In addition, the particles carry a location vector in physical space and compositional space. In the context of flamelet-based chemistry, this implies a four-dimensional vector denoted by $[\mathbf{x}^*, Z]$.

Particles evolve in physical space using filtered velocity and turbulence fields from the LES solver. Face-based velocities are interpolated onto particle positions using a trilinear interpolation algorithm. It was found that higher-order interpolation did not increase the accuracy of the computation nor ensure reduced statistical variability. Turbulent diffusivity is cell-center based and is again interpolated using a trilinear form. The Wiener diffusion process is simulated using a Gaussian random-number generator [39]. It is noted here that the equations of particle evolution (Eq. (24)) are in Cartesian coordinates. Since the LES solver uses cylindrical coordinates, the particle velocity is constructed by transforming the random walk component into a cylindrical form. This is easily achieved by first constructing the last term in the particle equation in Cartesian coordinates and then

using the metrics to transform it to cylindrical coordinates.

Due to the large number of particles involved, particle tracking has to be implemented efficiently. Here a face-to-face tracking strategy is used to move particles [18,40]. Given the initial position of a particle at a given time step, the nearest face based on the particle velocity is obtained. Then the time required to reach this face is computed. If the time required is more than the time step, the particle is moved to the final position within the same cell and tracking is completed. If the time required is less than the time step, the particle is moved to the face and the computation is repeated to find the nearest face (apart from the current face) in the next cell. The time step is reduced by the time already traveled in the previous cell. This procedure is repeated until the time step is reduced to zero or the particle moves out of the computational domain. The advantage of this scheme is the easy detection of solid boundaries. Since the boundaries lie on cell faces, particle boundary conditions are immediately applied and the velocity is appropriately modified. Here we use a no-slip condition which amounts to reflection of the normal component of the velocity.

Like the LES solver, the particle scheme also follows a domain-decomposition-based parallelization strategy. Although particles are tracked across processor boundaries, at the end of the transport step, all such particles that cross over into the next processor are collected and sent to the adjoining processors. Such transfers are two-way in that each processor needs to communicate with its neighbors to obtain and send crossover particles. Efficient particle data structures are used to communicate information across processors. It was found in the present study that the speedup of the computation scales linearly with number of processors up to 64 processors. It is expected that when finite-rate chemistry is added, the computational cost will increase significantly but the high degree of parallelism will still maintain tractability.

Transport in composition space is through mixing and reaction. Since laminar flamelet chemistry is used, the particle composition array has only a single species, namely the mixture fraction. Hence, the reaction source term is identically zero. The filtered mixture fraction field is obtained from the particle properties in a given cell as

$$\tilde{Z} = \frac{\sum_{i=1}^{N_p} w_i Z_i}{\sum_{i=1}^{N_p} w_i}. \qquad (36)$$

Micromixing is then implemented using Eq. (25) with the mixing time scale given by Eq. (22). It can be seen from Eq. (25) that when the time step is larger than the mixing time, the scalar values can become negative.

To ensure robustness, an analytical expression found by integrating Eq. (25) is used:

$$\boldsymbol{\phi}^{t+\Delta t} = \tilde{\boldsymbol{\phi}} + (\boldsymbol{\phi}^t - \tilde{\boldsymbol{\phi}})e^{-\frac{C_\phi \Delta t}{\tau}}. \tag{37}$$

Due to the statistical nature of the Lagrangian scheme, the accuracy of the method vastly depends on the sample size in a given computational cell. This is usually measured with regard to the particle number density. In a uniform Cartesian grid with constant-density fluid flow, the number of particles should stay uniform if the particles are distributed uniformly in the domain [2]. Here, a cylindrical coordinate system where the cell mass depends on the radial distance from the centerline is used. In addition, practical combustion calculations use extensive grid clustering to resolve regions of interest and to obtain stable converging solutions. In such scenarios, the particle number density can be treated independent of the local fluid and grid properties by using uneven particle weights [41]. Due to errors in interpolation and finite particle numbers, the instantaneous number density field contains large fluctuations. To reduce this variability, a number control algorithm is employed [18,40,41].

A nominal particle number density N_n is specified as a simulation parameter. At any time step, a number control algorithm is employed such that the number density in any cell is such that $N_n/5 < N < 3N_n$. The number control also makes use of the nominal particle weight given by $w_n = \bar{\rho}V_i/N_n$, where V_i is the volume of the cell. If the number density is higher than the tolerance level, then particles with weights less than w_n are identified and clustered until the number density reduces to the tolerance level. On the other hand, if the number of particles is less than the lower tolerance level, particles are split. In this case, each particle is split to identical particles but with weights equal to $1/N_{\text{split}}$ of the original particle, where N_{split} is the number of new particles formed. Similar to clustering, this process is carried out only until the tolerance level is reached. Clustering usually decreases the higher moments of the scalar and should be sparingly used.

The configuration studied here contains inflow/outflow boundaries that need to be handled consistently with the LES flow solver. At each step, the flux across each cell face is computed and a prescribed number of particles are introduced into the domain. Their locations are determined by using random velocities added to the filtered face velocity and by moving them inside from the face of the inflow for a time period equal to the time step. The composition vectors for these particles correspond to the inlet conditions for the scalar, with every particle from a particular inflow port carrying the same composition. The weight

of the particle is determined by the number of particles and the total flux across the face for the given time step.

The particle algorithm explained above was found to be highly efficient with the computational time of each particle step being almost equal to the computational time for the LES step.

3.3. Coupling algorithm

The LES flow solver and the particle-based FDF solver interact through the coupling algorithm. The forward transfer is simple in that the LES flow solver provides Favre-averaged face-centered velocity fields and the cell-centered turbulent diffusivity fields to the particle algorithm. The feedback part is more complex due to the stochastic noise inherent in filtered fields obtained from particles. As explained earlier, the enthalpy equation is used to obtain the filtered-density field for the LES flow solver. The FDF algorithm provides only the source term, for the enthalpy equation. This source term, given in Eq. (33), is computed from the particle field as

$$\widetilde{S}_h = \bar{\rho} \frac{1}{\sum_{i=1}^{N_p} w_i} \left[\sum_{i=1}^{N_p} w_i \frac{h_i^b - h_i^a}{\Delta t} \right], \tag{38}$$

where a and b refer to the enthalpy of the particle before and after the mixing substep, respectively. Using Eq. (30), the particle enthalpy can be directly computed from the flamelet table. This reaction source term is used to advance the equivalent enthalpy equation discretized using the QUICK scheme [36].

The rest of this article will detail the application of this hybrid approach to simulating a nonpremixed flame.

4. Application to a bluff-body-stabilized flame

4.1. Simulation details

The nonpremixed methane–hydrogen bluff-body-stabilized flame [24] is used to test the hybrid LES-FDF approach. The schematic of the flow configuration and the computational domain is provided in Fig. 2. The fuel is a methane–hydrogen mixture with 1:1 volume ratio entering through a pipe with diameter, D, of 3.6 mm. The coflow is air and enters through an annulus separated from the fuel by a solid bluff-body with a diameter of 50 mm. The experiments were performed at atmospheric pressure ($P_0 = 1$). Two different experimental configurations exist: the first termed HM1E was used to measure the velocity fields and the second termed HM1 was used for scalar measurement. Both flames have the same blowout
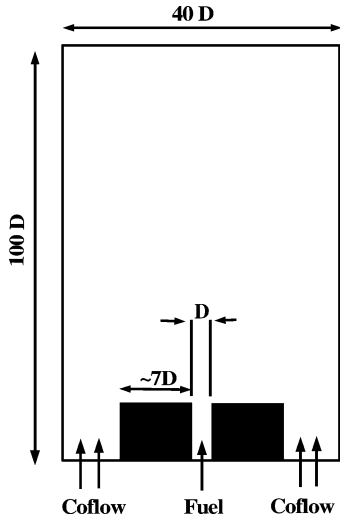
Fig. 2. Schematic of the bluff-body flame configuration. The jet diameter D is 3.6 mm.

characteristics, but the jet velocities are slightly different. HM1E was conducted with the fuel jet issuing at 108 m/s and coflow at 35 m/s. HM1 uses a fuel jet velocity of 118 m/s and coflow of 40 m/s. Here both configurations are simulated and compared with the corresponding experimental data.

In this study, a $256 \times 128 \times 32$ grid that spans $100D$ in the axial direction and $40D$ in the radial direction was used. The very low stoichiometric mixture fraction (≈ 0.055) necessitates high resolution in the outer shear layer to resolve the steep gradients in density. Similarly, the inner shear layer contains the strongest gradients in velocity and hence requires a finer grid to resolve the large scales. Consequently, the grid is heavily clustered in the inner shear layer and the outer vortex region, leading to large nonuniformities in particle weights. The primary reaction zone, where the flame reverts to a normal jet flame, is located at around $X = 65$ mm. Here again, the resolution of the grid is important. Although these observations are based on experimental data, no continuous adaptation of the grid is performed.

Due to the low extinction probability, the laminar flamelet model should adequately model combustion characteristics [25]. Here, the flamelet table is constructed using the FlameMaster code [42] with the mixture fraction and the mean scalar-dissipation rate as parameters. The GRI-2.11 chemistry mechanism [43] is used with the steady-flamelet equations [1]. The computational domain is sufficiently large to ensure that the flame characteristics are not affected by boundary conditions. The inlet conditions for the flow solver are obtained by storing a large number of velocity planes from a separate turbulent periodic pipe flow LES. This provides realistic time-correlated tur-

bulent inflow conditions that correlate well with the experimental data.

In the present study, a mixture-fraction-based flamelet model is used for describing the chemistry. For the Lagrangian solver, a single scalar, namely the mixture fraction, is evolved. For the sake of comparison, the mixture-fraction equation is also solved using an Eulerian scheme. To ensure that the second moment of the mixture fraction evaluated from the FDF scheme is accurate, an equivalent transport equation for the second moment is also solved in the Eulerian context. All the scalars use appropriate inflow conditions based on the species composition at the inlet plane. The outflow conditions are purely convective for both the momentum and the scalar equations. Further details of the LES solver are detailed elsewhere [32,37].

The FDF solver was initialized with 15 particles per cell. During the course of the simulation, the total number of particles in the domain was in the range of 10.5–21 million. The simulations were started from cold-flow-converged results after which the mixture was ignited using the flamelet solution. All simulations were continued for 7 flow-through times where each flow through time is defined as the time taken for a particle traveling along the centerline to move from inflow to exit. The simulation is time-averaged for 1.5 flow-through times starting at two different time steps separated by 1 flow-through time. The two time-averaged profiles differed by less than 2% for the mixture-fraction radial profiles, ensuring that statistical stationarity has been reached. The LES-FDF simulation took roughly 200 h on an eight-processor 600-MHz computer to reach statistical stationarity.

5. Results and discussion

The methane–hydrogen flame is stabilized by the two counter-rotating vortices seen in Fig. 3. The primary reaction zone is located at the end of the vortices, where the jet-like structure is recovered. The inner vortex helps to entrain the fuel into the recirculation zone. The outer vortex then preheats the coflow that comes in contact with the fuel in the center of the recirculation zone. Mixing is induced by these large-scale structures that are three dimensional with time scales an order of magnitude smaller than the mixing scales in the inner shear layer formed between the high-velocity fuel jet and the inner vortex. Such a large recirculation pattern aids mixing of reactants and leads to a near-uniform temperature. The thin shear layer separating the outer vortex from the coflow is a region of large reaction rates and serves as the primary ignition zone. Subfilter mixing is crit-
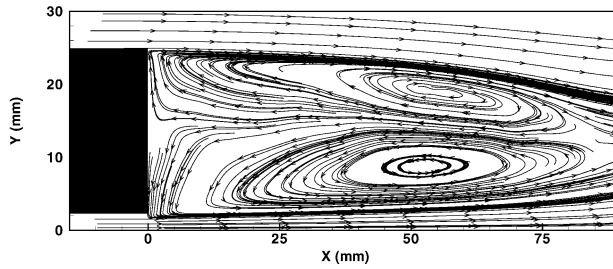
Fig. 3. Stream traces of the time-averaged velocity vector showing the counter-rotating vortices.
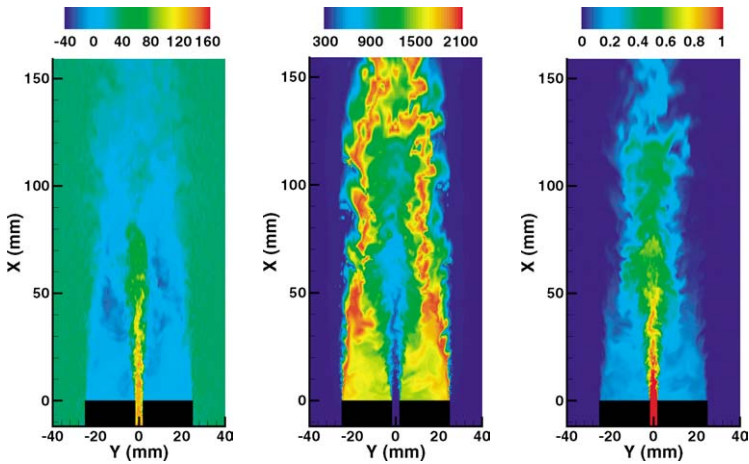

Fig. 4. Two-dimensional contour plots of instantaneous fields from the LES-FDF computation. (Left) velocity (m/s), (middle) temperature (K), and (right) mixture fraction.

ical in this region, since the fast chemistry leads to very small reaction length scales which are not resolved.

The instantaneous flow patterns are far more complex than the time-averaged stream traces (Fig. 4). In experiments, it has been observed that the outer surface of the bluff-body induces vortex shedding which interacts with the primary reaction zone [25]. Although the vortex shedding should depend on the inflow conditions used for the coflow, the time-averaged profiles for the scalars obtained using different coflow inlet profiles did not show significant differences. The effect of such vortex shedding on the reaction zone has been studied elsewhere [44].

The next few sections discuss the consistency, accuracy, and predictive capability of the hybrid scheme.

5.1. Consistency of the particle scheme

The consistency of the particle scheme can be assessed by comparing the density implied by the particle weights $\bar{\rho}_p$ and the density obtained from the particle compositions using the flamelet table $\bar{\rho}$. The Eulerian density field corresponding to the continu-

ity equation should be identical to $\bar{\rho}_p$ as implied by the FDF evolution equations. Fig. 5 shows the comparison of the three density fields at different axial positions. The Eulerian field and the particle-weights-based field are identical since the particle evolution is forced by the Eulerian density field. This serves to show that the numerical implementation is accurate. The comparison with the particle-composition-based density shows similar excellent agreement at all axial locations. This confirms that the feedback loop is accurate and that, despite the differences in the numerical algorithms for physical transport, both the Eulerian and the Lagrangian density fields agree with negligible differences.

5.2. Scalar PDF

The Lagrangian scheme has the unique feature that the PDF of the scalar is directly evolved. Here we compare this Lagrangian FDF with the presumed beta function. The FDF is constructed by time-averaging the instantaneous FDF in a computational cell for a short period of time. This approach reduces the statistical noise in the FDF. The beta function was constructed by time-averaging the presumed PDF eval-
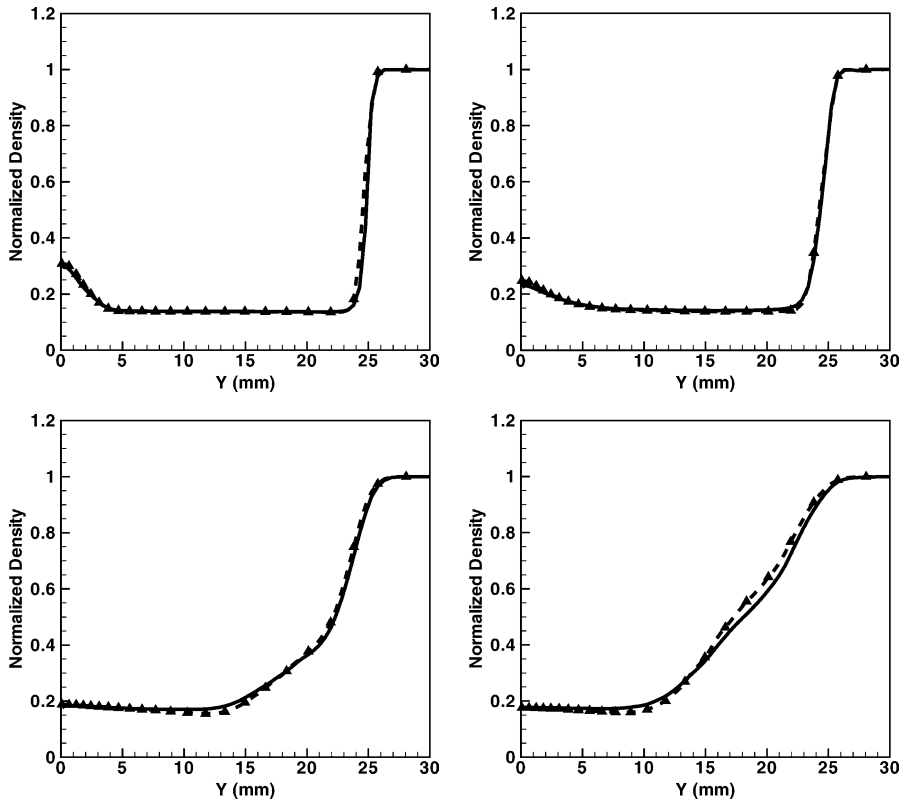
Fig. 5. Comparison of density obtained from particle weights (dashed line), particle composition (solid line), and LES flow solver (symbols). The four plots are at downstream locations of 13 and 30 (top), and 65 and 90 mm (bottom), respectively. The density values have been normalized by the density of the coflow.

uated using the instantaneous mean and variance at the location. The comparison at two different axial locations and at a given azimuthal angle are shown in Figs. 6 and 7. It is clear that, at all locations considered, the beta function approximates the PDF quite closely. The radial locations all lie on the inner or outer shear layers where mixing controls reaction. This result is not apparent from the FDF evolution equation (Eq. (19)), demonstrating the validity and consistency of the beta-function assumption for the PDF. Similar agreement was found at all azimuthal angles.

5.3. Velocity profiles

The time-averaged velocity obtained from simulation of HM1E is compared to the corresponding experimental data next. Radial profiles of the mean velocity profile are shown in Fig. 8. The axial-velocity profiles show very good agreement with experimental data at all locations. Similarly, the radial-velocity profiles show good agreement, but some discrepancies are observed especially at $X = 70$ mm. The axial-velocity profile at $X = 30$ mm indicates that the re-

circulation region is slightly overpredicted and the coflow velocity is not recovered. The same trend is noticed in the radial-velocity profiles where the second peak in the velocity is shifted outward, indicating that the shear layer is located further from the centerline. Further downstream, the axial-velocity profiles are in better agreement, with a slight underprediction near the centerline at $X = 70$ mm. This can be attributed directly to the coarser grid in the postcirculation zone. The radial-velocity profile consequently shows a higher discrepancy but predicts the trends quite accurately.

Fig. 9 shows the root mean square (RMS) of the velocity fluctuations. Here again, the axial-velocity component shows very good agreement with experimental data while the radial component shows some underprediction at downstream locations. The outer shear layer in the near-bluff-body region is characterized by vortex shedding, which will increase the velocity fluctuations. The peak in the experimental data at the end of the bluff-body ($Y = 25$ mm) indicates this behavior. The simulations are not likely to reproduce this peak since the exact nature of the vortex shedding and the physical cause of such a phe-
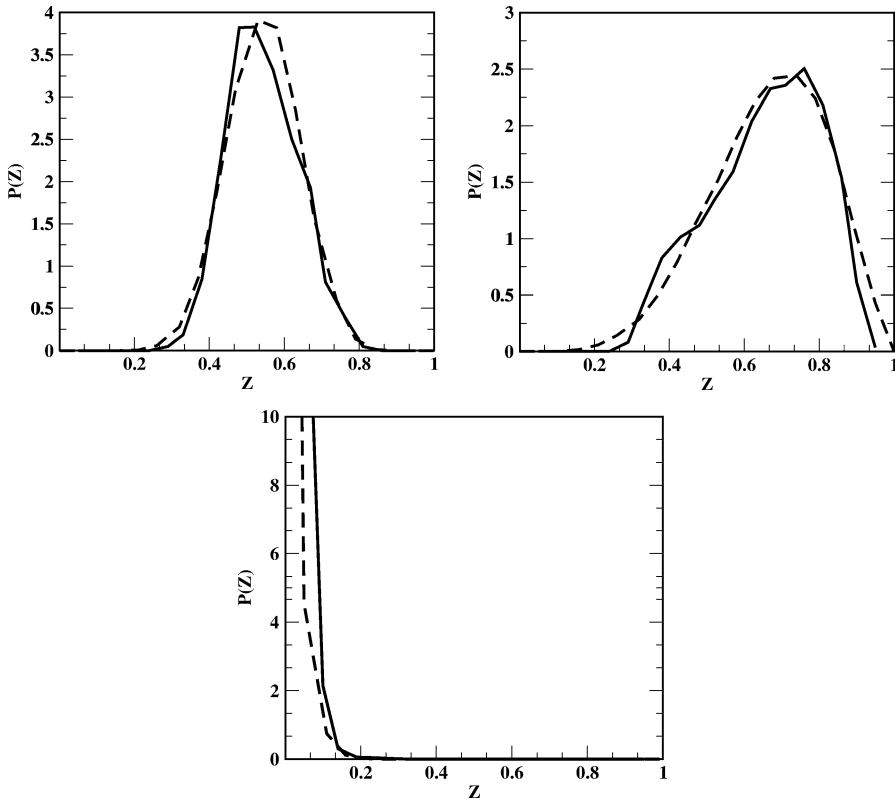
Fig. 6. Comparison of the probability density function of the mixture fraction obtained from the FDF solver (solid line) and a presumed beta function (dashed line) with the same mean and variance. The PDFs were computed at an axial position of 13 mm and at radial positions of 2.6, 3.6, and 20 mm.

nomenon needs to be modeled in the simulation. Here no such model was employed and, consequently, the minimal vortex shedding observed due to the inflow conditions was not strong enough to reproduce the secondary peak in the experimental data. In general, the profiles predict the correct trends in the flow and are quantitatively good considering the level of complexity of this flow.

The velocity profiles combined with the stream trace plots clearly show that the flame structure is captured quite accurately. Since the main region of interest is the recirculation zone for which the profiles match quite well, the faster jet decay at further downstream positions does not influence the flow structure. However, these results are better understood by considering the scalar and temperature profiles discussed next.

5.4. Scalar profiles

Figs. 10 and 11 show the time-averaged mixture fraction and RMS mixture fraction radial profiles at different axial locations. To aid in the comparison, the Eulerian mixture fraction and RMS mixture frac-

tion fields obtained from the finite-volume solution of the scalar transport equation are also included. It is observed that the mean mixture fraction profiles obtained from the FDF solver and the Eulerian solver show excellent agreement with one another and with the experimental data. The near-bluff-body profile shows a flat profile in the recirculation zone, further affirming the large-scale mixing in this region. The sharp decay of the mixture fraction near the edge of the bluff-body is a region of large temperature changes and consequently large density gradients. At $X = 30$ mm, the recirculation region is slightly over-predicted, indicated by the large mixture fraction values as compared to experiments and a sharper decay at the outer vortex, signifying a thin reaction zone. Further downstream the profiles are in much better agreement. At $X = 90$ mm, the profiles indicate a tendency of the flame to be narrower than the experimental observation. This is a direct consequence of the grid coarsening to limit the number of computational cells and leads to the faster decay of the axial velocity observed at $X = 70$ mm (Fig. 8).

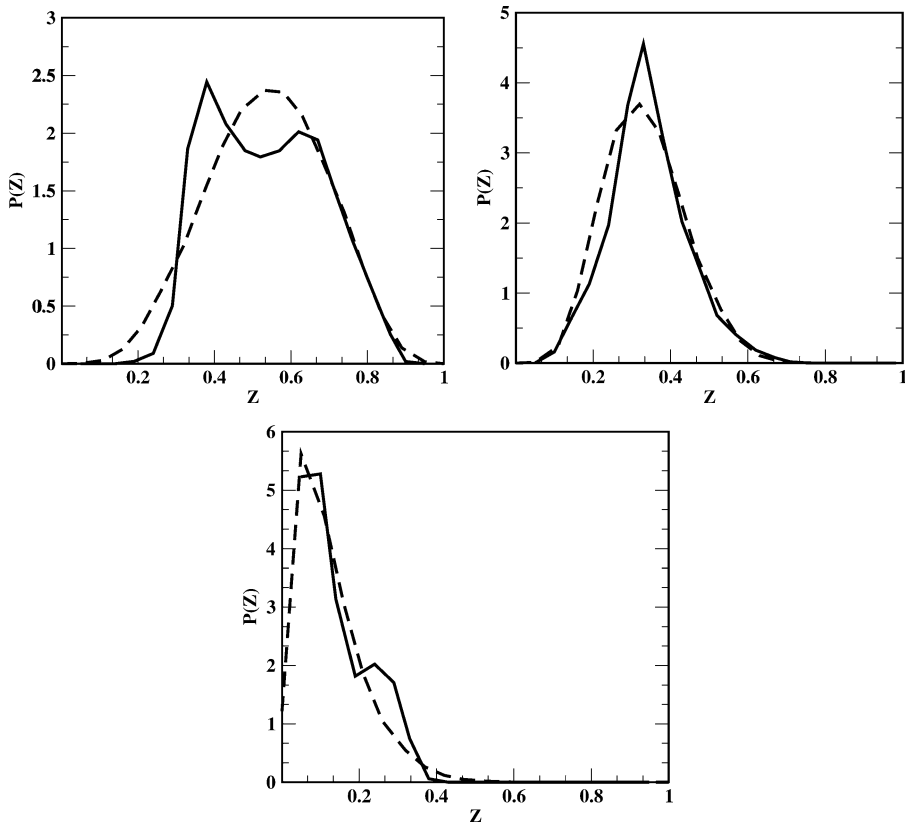The RMS profiles show good agreement with experimental data although certain discrepancies are no-

Fig. 7. Comparison of probability density function of the mixture fraction obtained from the FDF solver (solid line) and a presumed beta function (dashed line) with the same mean and variance. The PDFs were computed at an axial position of 65 mm and at radial positions of 2.8, 7.1, and 14.5 mm.

ticed near the centerline. In general, it is observed that the results agree well with the Eulerian computation also. At the first axial position considered, the FDF and Eulerian calculation show the right RMS profile, indicating that the large-scale recirculation has been captured accurately. It is noted that the subfilter or the unresolved variance in this zone is very small since the large-scale mixing renders the fluid homogeneous. Similar trends are observed at $X = 30$ and 45 mm, but the extent of the recirculation zone in the radial direction decreases as implied by the stream trace profile (Fig. 3). At $X = 65$ mm, the secondary peak in the mixture fraction RMS corresponding to the end of the recirculation zone is captured very accurately. Further downstream, the peak in the RMS profile is shifted toward the centerline which is consistent with the mixture fraction profiles that indicate a narrower jet spreading than the experimental observation.

It is observed that the RMS profiles from the FDF calculation at $X = 30$ and 45 mm show peaks near the centerline that are much larger than the experimental data. One explanation for this behavior is the reduction of accuracy of the particle tracking near the centerline. The LES solver uses a semiimplicit form, where the radial and azimuthal directions are treated implicitly and are hence independent of the CFL criteria accounting for the radial and azimuthal components. However, the particle method is fully explicit, implying that, in regions where the CFL criteria computed based on the radial or azimuthal velocity are not satisfied, the errors could be significant. It was found from an analysis of the turbulent-diffusivity profile that such an event is more likely to occur in the region where the central fuel jet breaks down. For this flow, this region varied from $X = 25$ to 60 mm. It is noted that the CFL criterion is not violated at each time step, but the additive errors due to frequent violation of this condition led to a spurious increase in the RMS fluctuation. Since the purpose of this study is to establish the hybrid technique as a viable tool for practical flows, no further evaluations are reported on this observation. Although not reported here, increase in the nominal particle number density decreased this error. Currently, a multistep fractional-stepping algorithm is being tested to overcome this problem.
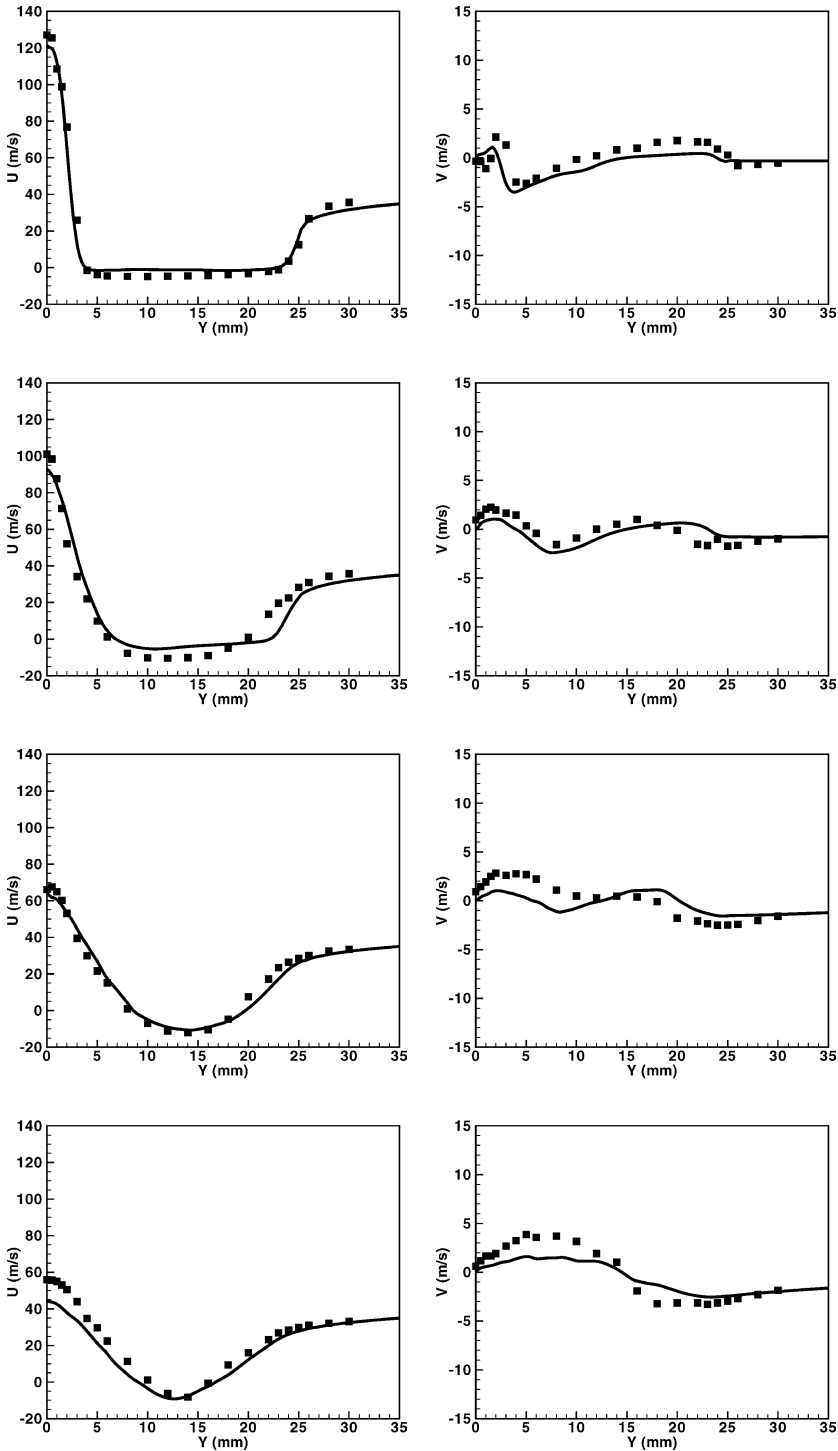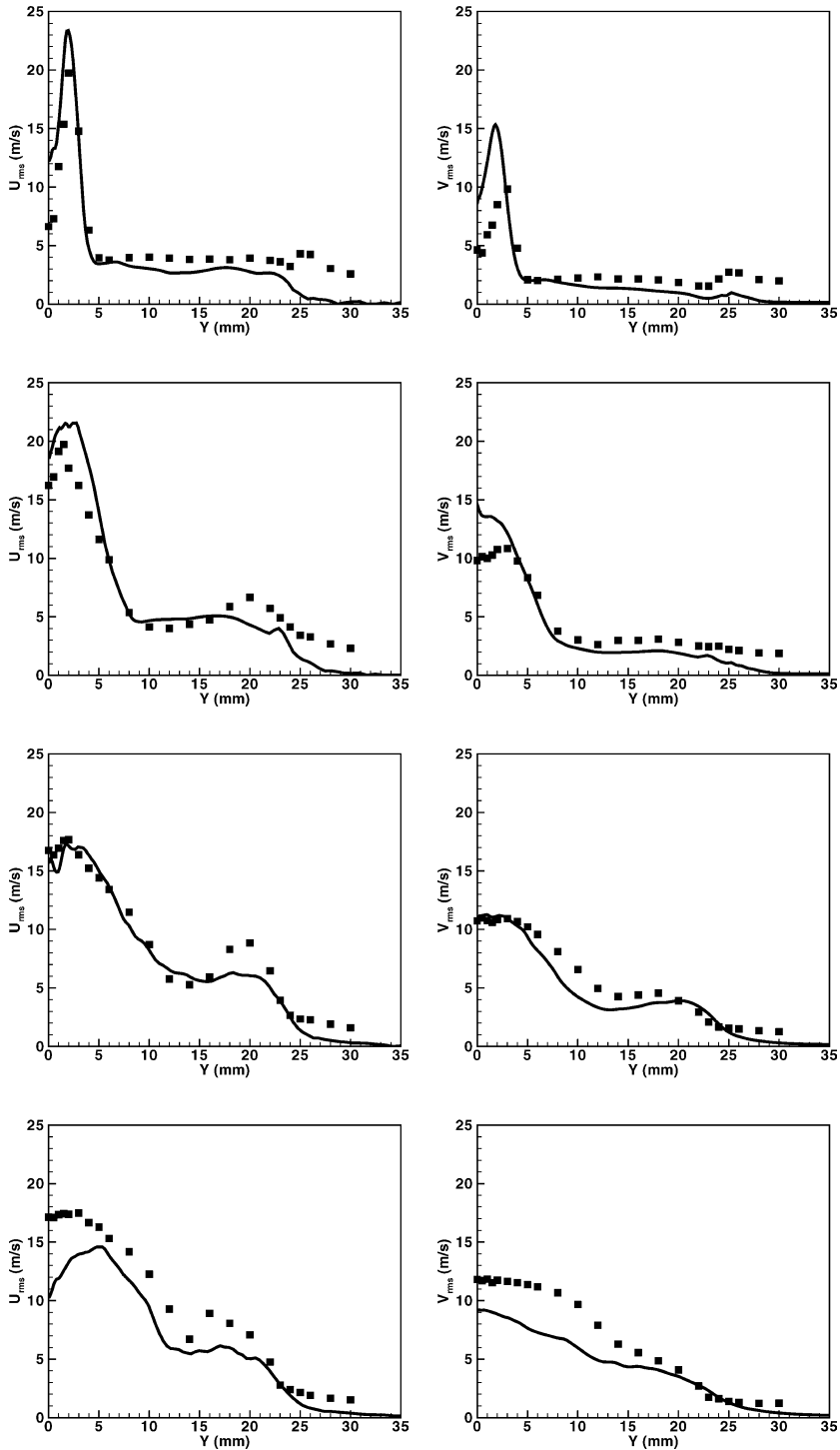
Fig. 8. Comparison of axial (left) and radial (right) velocity with experimental data at different axial locations. From top to bottom, $X = 10$, 30, 50, and 70 mm. Symbols are experimental data; lines show simulation results.

Figs. 12 and 13 show the radial profiles of temperature and CO_2 mass fraction. From the plots, it is evident that both scalars behave similarly in this

flame. Similar to the mixture fraction profiles, the mean temperature and species mass fraction exhibit close agreement with experimental data in regions

Fig. 9. Comparison of RMS of axial (left) and radial (right) velocity fluctuations with experimental data at different axial locations. From top to bottom, $X = 10$, 30, 50, and 70 mm. Symbols are experimental data; lines show simulation results.

close to the bluff-body. At downstream locations of $X = 45$ and 65 mm, the peak in the temperature is underpredicted. These regions correspond to the outer

shear layer and regions of maximum reaction rate. At $X = 45$ mm, the mean and RMS mixture fraction are accurately predicted in the outer shear layer. Hence,
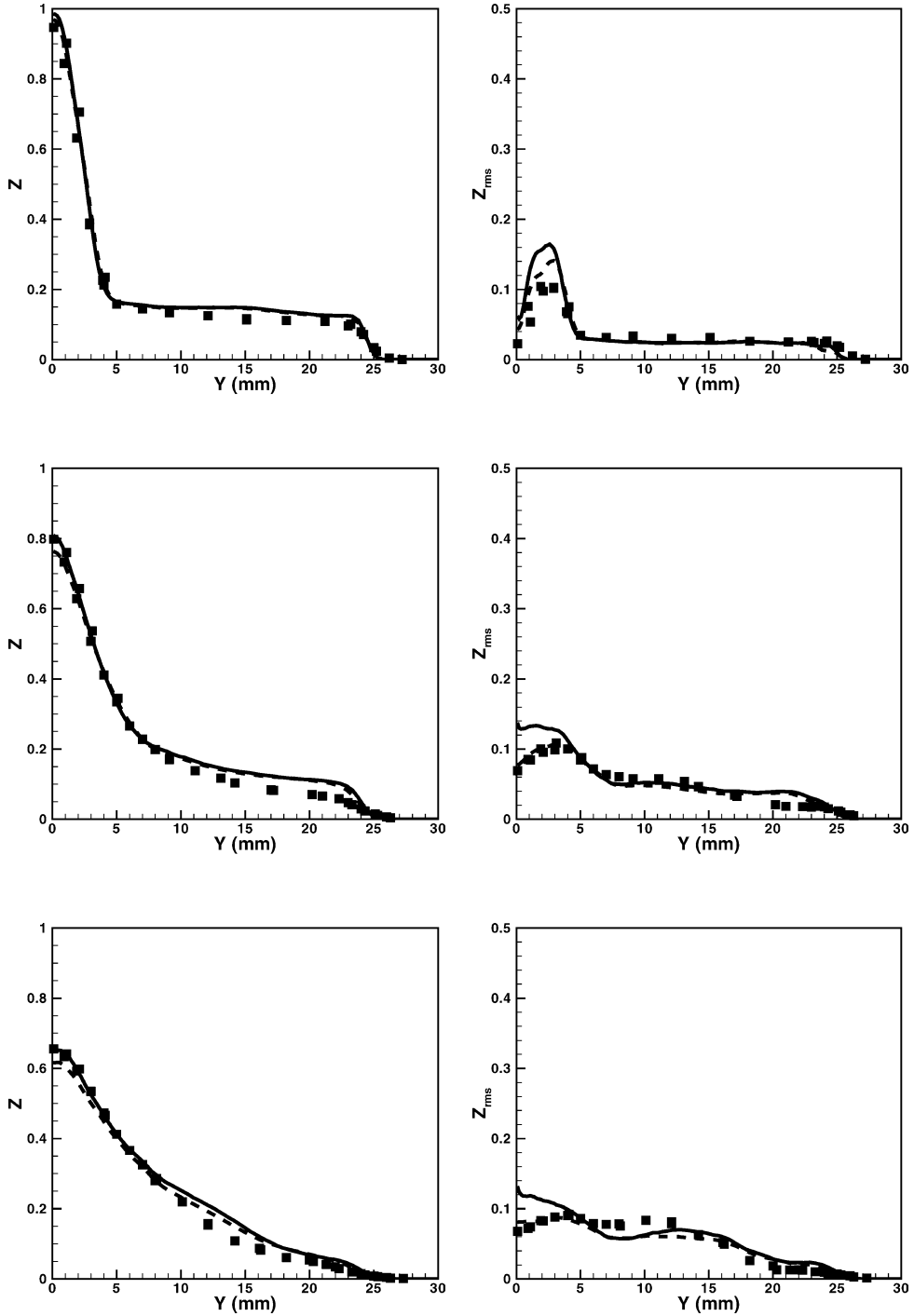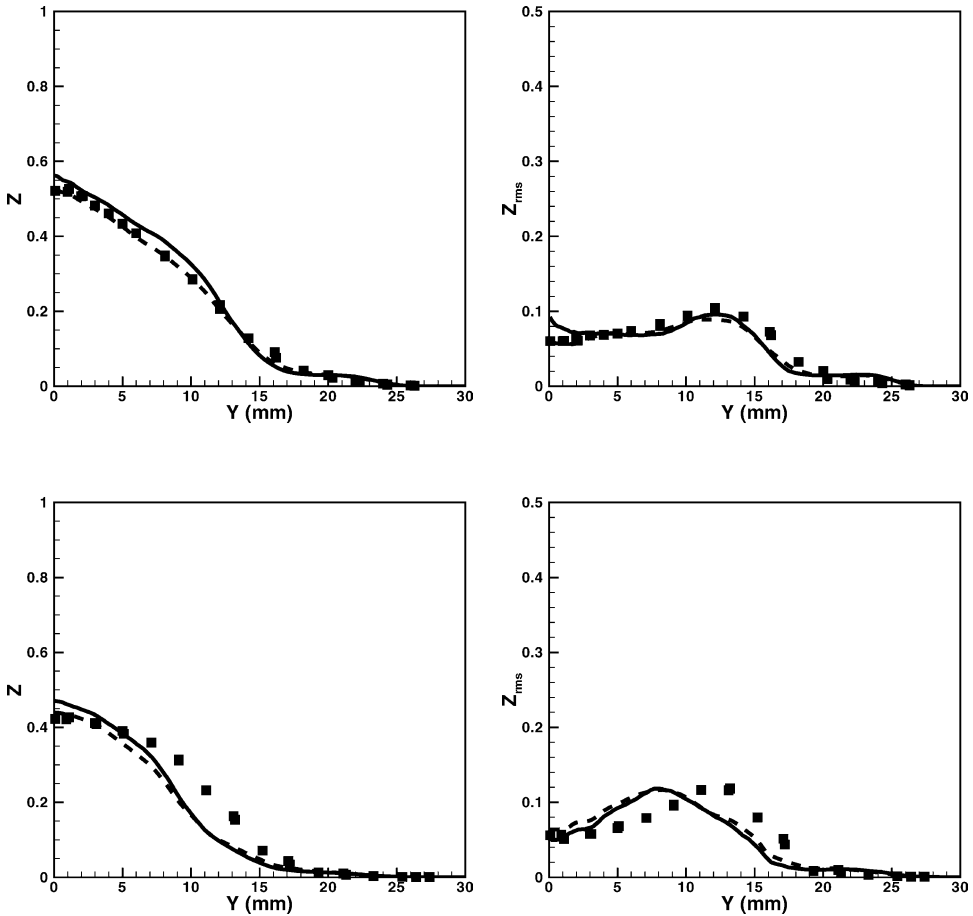
Fig. 10. Comparison of mean mixture fraction and RMS mixture fraction profiles with experimental data at different axial locations. From top to bottom, $X = 13$, 30, and 45 mm. Symbols are experimental data; solid lines show FDF-based results; dashed lines show beta-function-based Eulerian calculation.

the discrepancy can be attributed to the subfilter mixing model. In this work, a simple IEM closure is used to describe micromixing along with a turbulent-

diffusivity-based time scale. Since the beta-function-based evaluation shows the same underprediction, the general shape of the subfilter PDF is not the deter-

Fig. 11. Comparison of mean mixture fraction and RMS mixture fraction profiles with experimental data at different axial locations. From top to bottom, $X = 65$ and 90 mm. Symbols are experimental data; solid lines show FDF-based results; dashed lines show beta-function-based Eulerian calculation.

mining factor. This is directly observed from Figs. 6 and 7 which show that the beta function accurately reproduces the FDF in the outer vortex region. Hence, it is concluded that the subfilter mixing rate is underpredicted, leading to larger subfilter variance. This could lead to an underprediction of the reaction rate which is observed in the lower peak temperature. This trend is observed at other downstream locations also. The CO_2 mass fraction profiles indicate identical trends.

Figs. 14 and 15 show the radial profiles of CO and OH mass fractions. Considering the simplicity of the chemistry model, the CO profiles show good agreement with experimental data. Prediction of OH profiles in any combustion simulation is particularly challenging due to the strong nonlinearity of the species evolution. At $X = 13$ mm, the production is limited to the outer shear layer. The FDF scheme predicts this peak quite accurately but the Eulerian scheme shows a pronounced peak. Looking at the temperature profile at this location (Fig. 12), a small

spike is noticed at the outer edge of the bluff-body. This clearly results in the overprediction of the hydroxyl radical. This inaccuracy is a result of the numerical scheme used, as it is well known that the QUICK discretization scheme contains some spurious oscillations in regions of large scalar gradients [32]. Typically, central-difference-based numerical discretization schemes will contain some level of oscillations [36]. At $X = 30$ and 45 mm, the FDF and Eulerian predictions agree well with experiments. The reaction zone also widens compared to $X = 13$ mm. Similar trends are observed at $X = 65$ and 90 mm.

6. Conclusions

A consistent stable algorithm for hybrid LES-FDF simulations has been devised and implemented. The low-Mach-number-approximation-based LES solver was coupled to the notional-particle-based Lagrangian
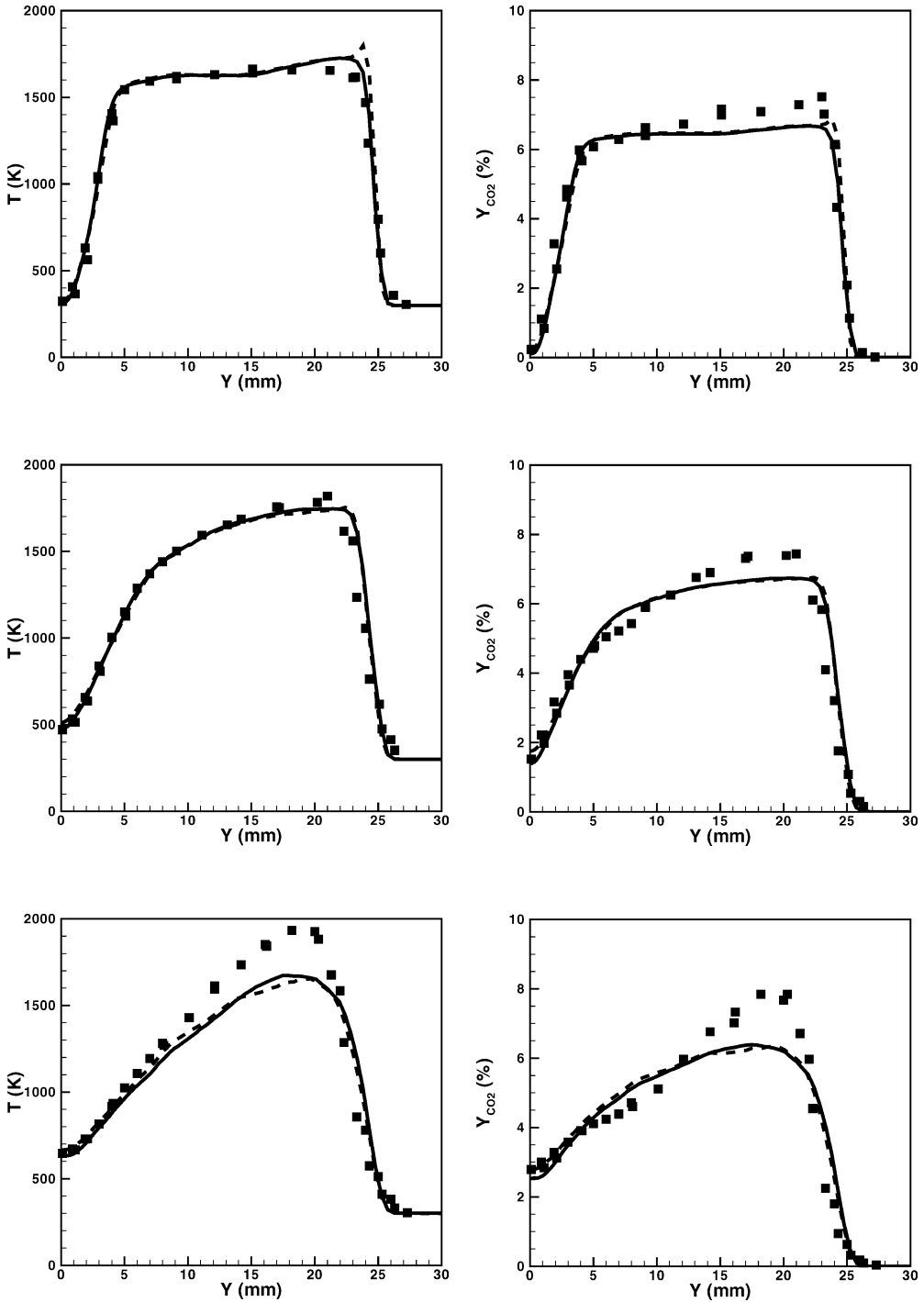
Fig. 12. Comparison of mean temperature and CO_2 mass fraction profiles with experimental data at different axial locations. From top to bottom, $X = 13$, 30, and 45 mm. Symbols are experimental data, solid lines show FDF-based results; dashed lines show beta-function-based Eulerian calculation.

FDF solver using a time-accurate coupling scheme. The particle scheme was implemented using scalable algorithms with distributed-memory-based parallelism. Linear scaleup was obtained up to 64 processors. Particle motion in physical space was implemented using a cell-faced tracking strategy. In com-
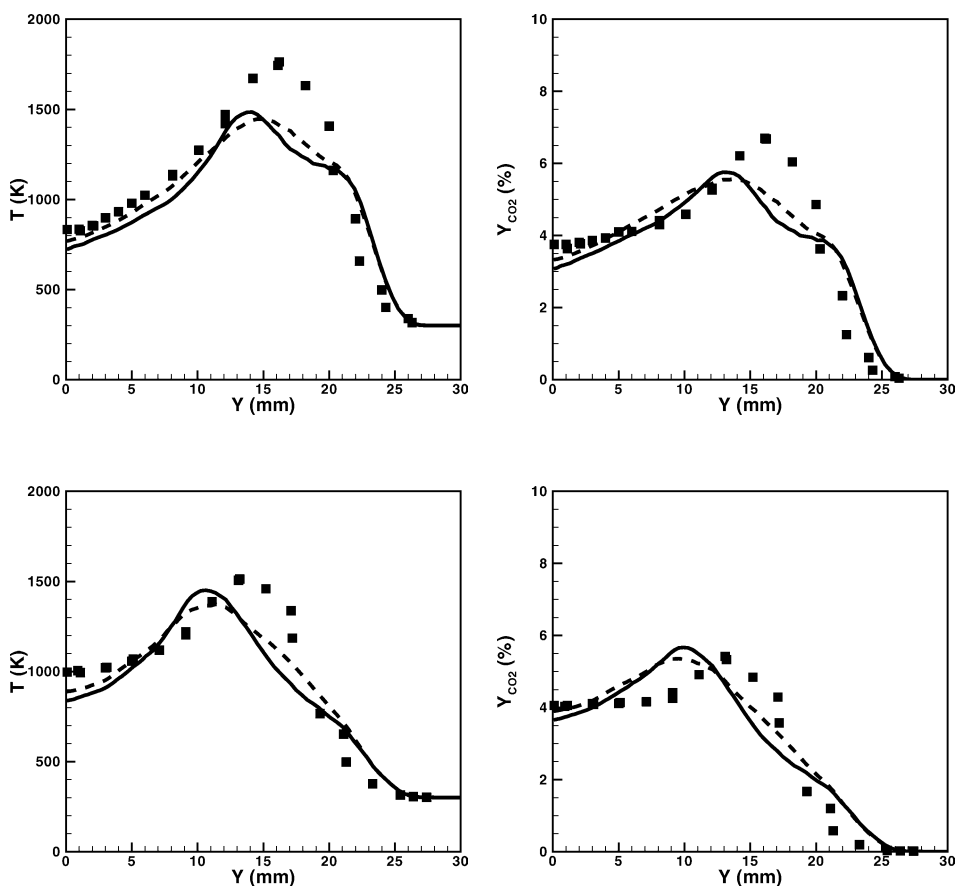
Fig. 13. Comparison of mean temperature and CO_2 percentage mass fraction profiles with experimental data at different axial locations. From top to bottom, $X = 65$ and 90 mm. Symbols are experimental data; solid lines show FDF-based results; dashed lines show beta-function-based Eulerian calculation.

position space, particles were moved through mixing and reaction. A simple IEM model with a turbulent-diffusivity-based time scale was used for describing mixing. Since a mixture fraction-based flamelet approach is used, the reaction source term was set to zero.

The coupling algorithm between the solvers is nontrivial in the LES-FDF approach as compared to a RANS-PDF approach to time-dependent evolution of the flow. The particle velocities are updated using velocity fields from the LES solver at every time step. The chemical reaction information is supplied to the flow field indirectly through density changes. Since the particle solver uses a statistical method, direct feedback of particle mean fields contain stochastic noise which can lead to numerical instabilities. To overcome this issue, an equivalent enthalpy equation is used with the particle scheme supplying the exact source term for the Eulerian transport equation of this quantity. This feedback algorithm is found to ensure numerical stability.

The LES-FDF approach has been applied to a challenging nonpremixed flame configuration. The methane–hydrogen-fueled bluff-body-stabilized flame exhibits complex flow structures that require time-dependent evolution of the flow field. The LES-FDF scheme was used to simulate this configuration using a reasonably refined computational grid and approximately 15 million particles. Several features of the algorithm including consistency and accuracy were established by comparing redundant fields on the particle and LES sides of the algorithm. The comparison with a presumed function for the PDF of the scalar compared well with the FDF approximation.

The species profiles show that the simple laminar flamelet model is able to predict the experimental data quite accurately. The comparison with the mixture fraction field evolved using an Eulerian scheme showed very good agreement with the FDF scheme, verifying the accuracy of the FDF algorithm. The predictions of scalar profiles were consistently good, mainly due to the very good prediction of the filtered
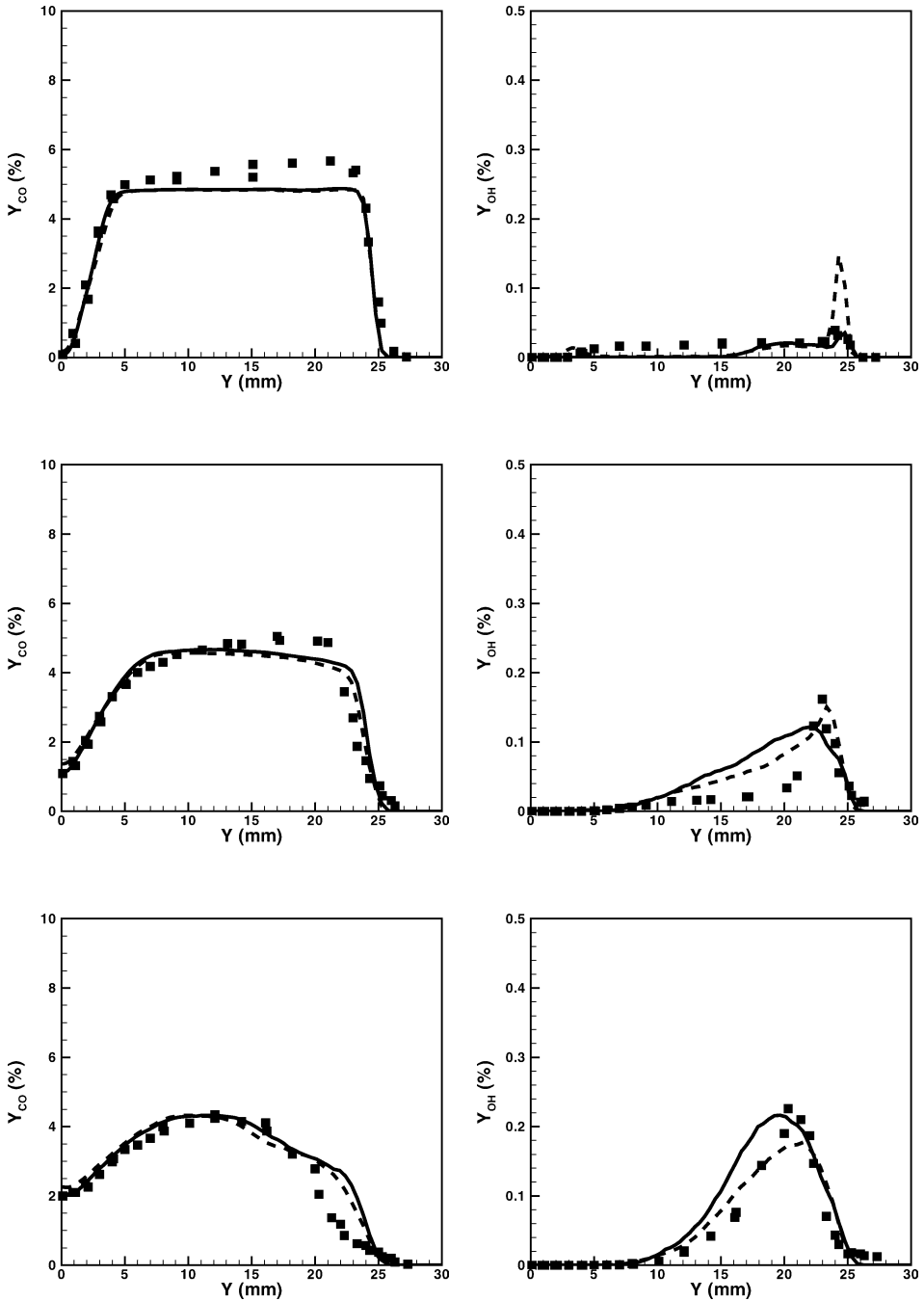
Fig. 14. Comparison of mean CO and OH mass fraction profiles with experimental data at different axial locations. From top to bottom, $X = 13$, 30, and 45 mm. Symbols are experimental data; solid lines show FDF-based results; dashed lines show beta-function-based Eulerian calculation.

mixture fraction and the mixture fraction RMS. For this flame with low levels of extinction, the mixing model was found to play an important role in the thin reaction zone separating the coflow from the outer vortex of the recirculation zone. The current study establishes the viability and fidelity of the LES-FDF scheme. The real advantage of this hybrid approach is the direct closure of the chemical source terms. This feature has not been exploited here and will be the focus of future work.
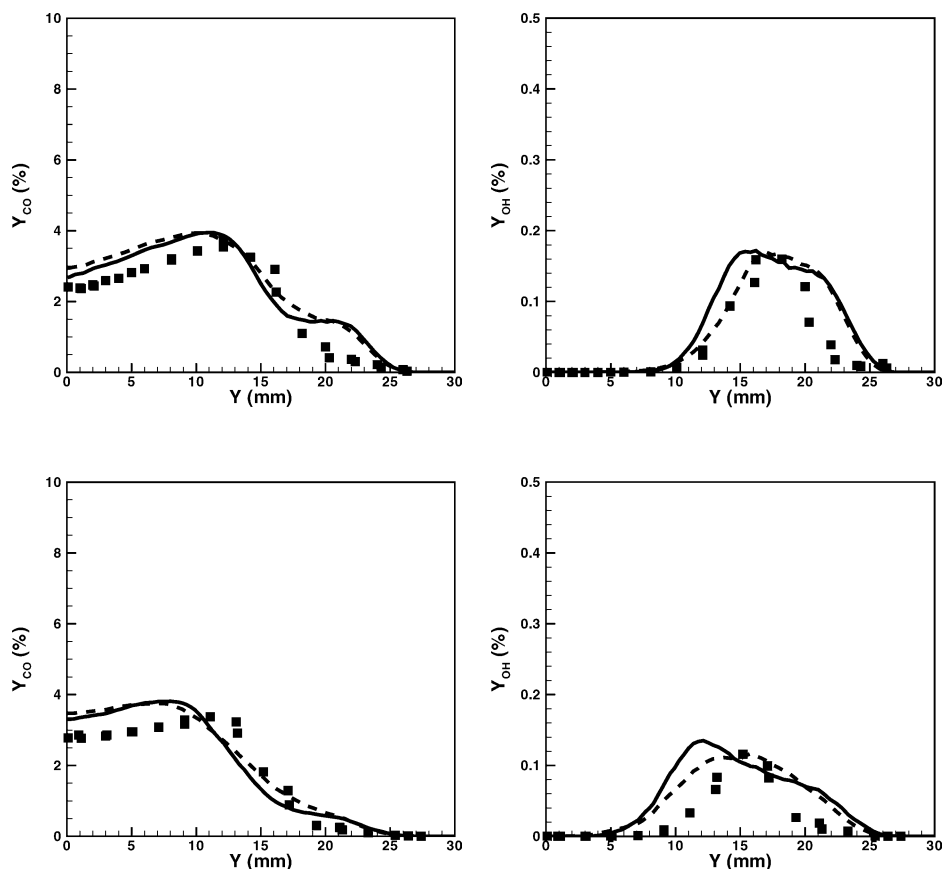
Fig. 15. Comparison of mean CO and OH mass fraction profiles with experimental data at different axial locations. From top to bottom, $X = 65$ and 90 mm. Symbols are experimental data; solid lines show FDF-based results; dashed lines show beta-function-based Eulerian calculation.

References

[1] N. Peters, Turbulent Combustion, Cambridge Univ. Press, Cambridge, UK, 2000.

[2] S.B. Pope, Turbulent Flows, Cambridge Univ. Press, Cambridge, UK, 2000.

[3] H. Pitsch, H. Steiner, Phys. Fluids 12 (10) (2000) 2541–2554.

[4] A.W. Cook, J.J. Riley, Phys. Fluids 10 (1994) 499–515.

[5] R.W. Bilger, Phys. Fluids 5 (2) (1993) 436–444.

[6] A.Y. Klimenko, Phys. Fluids 7 (2) (1995) 446–448.

[7] S.H. Kim, K.Y. Huh, Combust. Flame 130 (1–2) (2002) 94–111.

[8] S.B. Pope, Combust. Sci. Technol. 25 (1981) 159–174.

[9] S.B. Pope, Progr. Energy Combust. Sci. 11 (1985) 119.

[10] S.B. Pope, Annu. Rev. Fluid Mechan. 26 (1994) 23–63.

[11] R.L. Curl, AIChE J. 9 (1963) 175–181.

[12] J. Villermaux, L. Falk, Chem. Eng. Sci. 49 (24B) (1994) 5127–5140.

[13] J. Janicka, W. Kolbe, W. Kollmann, J. Non-Equilibr. Thermodyn. 4 (1970) 47–66.

[14] S. Subramaniam, S.B. Pope, Combust. Flame 117 (1999) 732.

[15] R.O. Fox, Phys. Fluids 6 (1994) 334.

[16] R.O. Fox, Computational Models for Turbulent Reacting Flows, Cambridge Univ. Press, Cambridge, UK, 2003.

[17] S.M. Correa, S.B. Pope, Comparison of a Monte Carlo PDF finite-volume mean flow model with bluff-body Raman data, in: Twenty-Fourth International Symposium on Combustion, Combustion Institute, Pittsburgh, 1992, pp. 279–285.

[18] V. Raman, R.O. Fox, A.D. Harvey, Combust. Flame 136 (2004) 327–350.

[19] M. Muradoglu, K. Liu, S.B. Pope, Combust. Flame 132 (1–2) (2003) 115–137.

[20] P. Jenny, S.B. Pope, M. Muradoglu, D.A. Caughey, J. Comput. Phys. 166 (2001) 218–252.

[21] P.J. Colucci, F.A. Jaberi, P. Givi, Phys. Fluids 10 (2) (1998) 499–515.

[22] F.A. Jaberi, P.J. Colucci, S. James, P. Givi, S.B. Pope, J. Fluid Mechan. 401 (1999) 85–121.

[23] L.Y.M. Gicquel, P. Givi, F.A. Jaberi, S.B. Pope, Phys. Fluids 14 (3) (2002) 1196–1213.

[24] B.B. Dally, A.R. Masri, R.S. Barlow, G.J. Fietchner, Combust. Flame 114 (1998) 119–148.

[25] B.B. Dally, D.F. Fletcher, A.R. Masri, Combust. Theory Model. 2 (1998) 193–219.

[26] J. Smagorinsky, Mon. Weather Rev. 91 (1963) 99–164.
[27] J. Bardina, J.H. Ferziger, W.C. Reynolds, AIAA J. (1980) 80–1357.
[28] M. Germano, J. Fluid Mechan. 286 (1991) 229–255.
[29] P. Moin, K. Squires, W. Cabot, S. Lee, Phys. Fluids A 3 (1991) 2746–2757.
[30] S. Ghosal, T.S. Lund, P. Moin, K. Akselvoll, J. Fluid Mechan. 286 (1995) 229–255.
[31] C.D. Pierce, P. Moin, J. Fluid Mechan. 504 (2004) 73–97.
[32] C.D. Pierce, Progress-variable approach for large-eddy simulation of turbulence combustion, Ph.D. thesis, Stanford University, 2001.
[33] K. Tsai, R.O. Fox, Indust. Eng. Chem. Res. 37 (6) (1998) 2131–2141.
[34] M. Muradoglu, P. Jenny, S.B. Pope, D.A. Caughey, J. Comput. Phys. 154 (1999) 342–371.
[35] C.D. Pierce, P. Moin, Phys. Fluids 10 (1998) 3041–3044.
[36] B.P. Leonard, Comput. Methods Appl. Mechan. 19 (1979) 59–98.
[37] K. Akselvoll, P. Moin, J. Fluid Mechan. 315 (1996) 387–411.
[38] J. Jimenez, A. Linan, M.M. Rogers, F.J. Higuera, J. Fluid Mechan. 349 (1997) 149–171.
[39] W.H. Press, S.A. Teukolsky, W.T. Vetterling, B.P. Flannery, Numerical Recipes in Fortran 77, Cambridge Univ. Press, Cambridge, UK, 1992.
[40] S. Subramaniam, D. Haworth, Int. J. Engine Res. 1 (2000) 171–190.
[41] D.C. Haworth, S.H. El Tahry, AIAA J. 29 (2) (1991) 208–218.
[42] H. Pitsch, A C++ Computer Program for 0-d and 1-d Laminar Flame Calculations, rWTH Aachen, 1998.
[43] C.T. Bowman, R.K. Hanson, D.F. Davidson, et al., Grimech 2.11, 1995 available at: http://www.me.berkeley.edu/gri_mech/.
[44] V. Raman, H. Pitsch, Combust. Flame (2005), accepted for publication.